Counting the Number of Magnesium Ions Bound to the Surface-Immobilized Thymine Oligonucleotides That Comprise Spherical Nucleic Acids
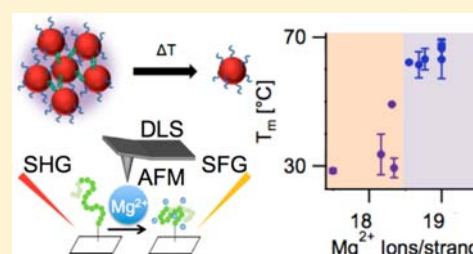
Stephanie R. Walter,[†,‡] Kaylie L. Young,[†,‡] Joseph G. Holland,[†,‡] Richard L. Gieseck,[†,‡] Chad A. Mirkin,[†,‡] and Franz M. Geiger*,[†,‡]

[†]Department of Chemistry, Northwestern University, Evanston, Illinois 60208, United States
[‡]International Institute for Nanotechnology, Northwestern University, Evanston, Illinois 60208, United States

S Supporting Information

ABSTRACT: Label-free studies carried out under aqueous phase conditions quantify the number of Mg^{2+} ions binding to surface-immobilized T_{40} sequences, the subsequent reordering of DNA on the surface, and the consequences of Mg^{2+} binding for DNA−DNA interactions. Second harmonic generation measurements indicate that, within error, 18−20 Mg^{2+} ions are bound to the T_{40} strand at saturation and that the metal−DNA interaction is associated with a near 30% length contraction of the strand. Structural reordering, evaluated using vibrational sum frequency generation, atomic force microscopy, and dynamic light scattering, is attributed to increased charge screening as the Mg^{2+} ions bind to the negatively charged DNA, reducing repulsive Coulomb forces between nucleotides and allowing the DNA single strands to collapse or coil upon themselves. The impact of Mg^{2+} binding on DNA hybridization and duplex stability is assessed with spherical nucleic acid (SNA) gold nanoparticle conjugates in order to determine an optimal working range of Mg^{2+} concentrations for DNA−DNA interactions in the absence of NaCl. The findings are consistent with a charge titration effect in which, in the absence of NaCl, (1) hybridization does not occur at room temperature if an average of 17.5 or less Mg^{2+} ions are bound per T_{40} strand, which is not reached until the bulk Mg^{2+} concentration approaches 0.5 mM; (2) hybridization proceeds, albeit with low duplex stability having an average T_m of 31(3)°C, if an average of 17.5−18.0 Mg^{2+} ions are bound; and (3) highly stable duplexes having a T_m of 64(2)°C form if 18.5−19.0 Mg^{2+} ions are bound, corresponding to saturation of the T_{40} strand.

1. INTRODUCTION

The molecular recognition properties of DNA have inspired applications ranging from DNA sequencing,[1,2] gene expression profile mapping,[3,4] large-scale screening of genetic mutations and biomarkers,[5−7] the separation of biomolecules in complex mixtures,[8,9] intracellular detection of mRNA in live cells,[10] and intracellular gene regulation.[11,12] In addition, they have led to the concept of programmable matter in the form of DNA origami[13,14] and colloidal crystals.[15−17] The latter has catalyzed an entire new field with emerging design rules for creating periodic lattices from nanoparticles functionalized with DNA that behave as programmable atom equivalents.[18,19] Many of these uses rely on the successful hybridization of surface-bound DNA capture strands to target sequences. Despite the use of oligonucleotides in the applications listed above, the interactions of surface-bound DNA with its environment are not easily monitored directly, and little is known about how the reaction conditions (e.g., electrolyte concentrations) impact interfacial DNA structure and target-capture efficiency.

The presence of salt is central to DNA hybridization, with typical protocols involving NaCl concentrations in the hundreds of millimolar range or divalent cation concentrations of a few millimolar. We focus on surface-bound DNA interactions with magnesium ions since magnesium is important for a multitude of biochemical interactions and is often present in the media and buffer solutions used for DNA-based applications.[20−24] Previous studies have shown that magnesium binds to DNA and can affect DNA structure in solution.[25−27] Magnesium binding can occur through the N7 site of purines and N3 site of pyrimidines, and/or through the phosphate group along the DNA backbone without blocking the base sites that are required for hybridization.[27−29] Additionally, the presence of magnesium is well-known to stabilize DNA duplexes in solution.[28,30−33] Melting temperature (T_m) increases have been observed until Mg^{2+} concentrations of 10−100 mM are reached, beyond which T_m values become invariant with Mg^{2+} concentration;[32,34−36] however, surprisingly little is known about how many Mg^{2+} ions interact with a given oligonucleotide strand at an interface. The number of metal cations bound to DNA can be counted if an X-ray crystal structure is available,[25] but doing so in aqueous solution is currently a challenge. Previous experiments provide little information on the effects of magnesium on surface-bound

DNA structure, how many magnesium ions are bound per strand, or assess what concentration regimes are relevant for duplex formation and stability. An optimized working range of salt concentrations is particularly important when working with colloidal assays as aggregation and precipitation can occur at high salt concentrations. Furthermore, SNAs (spherical gold nanoparticle constructs with a dense layer of highly oriented nucleic acids) have a high local salt concentration relative to the bulk solution, which may significantly impact cellular uptake and binding activities for which they are designed.[37,38]

Herein, we report a label-free method to effectively quantify the number of Mg^{2+} ions interacting with surface-bound oligonucleotides, and determine the implications of Mg^{2+} ion binding for DNA hybridization and duplex stability. To detail the Mg^{2+} ion−DNA binding strength, strand loading, degree of structural order/disorder resulting from surface-bound DNA interactions with Mg^{2+}, and the subsequent implications for DNA−DNA interactions, we employ nonlinear surface-specific spectroscopies, namely, second harmonic generation (SHG) and sum frequency generation (SFG), along with dynamic light scattering (DLS) and atomic force microscopy (AFM) experiments, and SNA gold nanoparticle conjugate assays. Together, our results constitute the first experimental quantification of how many Mg^{2+} ions interact with surface-bound DNA under aqueous phase conditions, and link the Mg^{2+} strand loading with duplex stability measurements aimed at rationalizing the working range of Mg^{2+} concentrations for NaCl-free surface-bound DNA hybridization.

2. EXPERIMENTAL METHODS

The DNA strand employed in this study is a 40-mer thymine sequence (T_{40}) covalently bound to fused silica and gold nanoparticle surfaces. We specifically chose a thymine-based oligonucleotide since such sequences are employed for mRNA separation and extraction processes,[8,9,39] wherein thymine-functionalized microbeads are used to selectively hybridize and isolate the poly(A) tail that is unique to mRNA. SFG and SHG are uniquely suited for the analysis of surface-bound DNA[40,29,41−45] as these coherent spectroscopies are non-destructive, label-free, and surface-specific with high sensitivity for *in situ* analysis under aqueous conditions. AFM further complements our nonlinear optical studies by directly imaging subnanometer topographical features of DNA-functionalized surfaces undergoing magnesium binding interactions under aqueous conditions.[46−53] Finally, SNA gold nanoparticle conjugates (SNA-AuNP) are studied to assess real-time hybridization and duplex stabilization in the presence of magnesium ions.

2.1. Materials. T_{40} sequences of DNA with terminal amine-modifications were purchased from IDT DNA Technologies and Sigma Aldrich and used without further purification. Oligonucleotides for the nanoparticle hybridization studies were synthesized on an MM48 Synthesizer (Bioautomation) using standard solid-phase phosphoramidite chemistry. Bases and reagents were purchased from Glen Research Co. and oligonucleotides were purified by reverse-phase high performance liquid chromatography (HPLC, Varian). Thirty nanometer gold nanoparticles were purchased from Ted Pella. Deuterium oxide (DLM-2259-100) was purchased from Cambridge Isotope Laboratories. IR-grade fused-silica windows (QI-W-25-3) for SFG and UV-grade fused-silica hemispheres (QU-HS-25) for SHG were purchased from ISP Optics. AFM substrates consisted of heavily boron doped Si wafers with 300 nm of thermally grown silicon oxide from WRS Materials. All other materials were purchased from Sigma Aldrich unless otherwise stated.[29,44,45,54] UV−vis data were obtained on a Cary 5000 UV−vis-NIR spectrophotometer (Varian Inc., CA, USA).

2.2. DNA Functionalization on Silica. The functionalization procedure used to covalently attach oligonucleotides to silica surfaces
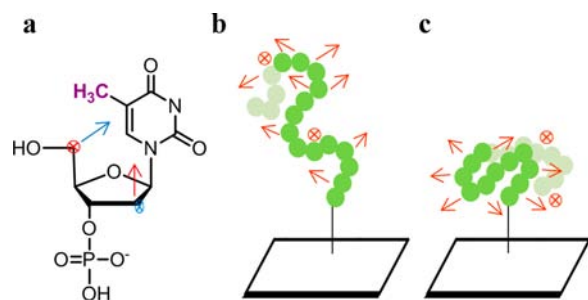
has been published previously.[45] Briefly, fused-silica windows and hemispheres were cleaned for 1 h in a Nochromix solution, rinsed with Millipore H_2O (Milli-Q system), sonicated in methanol, dried with N_2, and plasma cleaned for 2−5 min. SiO_2/Si wafers were sonicated in methanol for 10 min then plasma cleaned for 2−5 min. A linker of 11-(trichlorosilyl)-undecanoic acid *N*-hydroxysuccinimide (NHS) ester was synthesized and deposited onto the cleaned silica substrates in an inert atmosphere glovebox and then annealed for 1 h at 100 °C in an oven. Following NHS-linker deposition, a 10 μM solution of amine-terminated T_{40} in 0.1 M sodium borate buffer (pH 9) was pipetted over the substrate and allowed to react with the NHS-linker overnight. The amine-modification on the T_{40} sequence reacts with the NHS ester to covalently link the DNA to the surface via amide bond formation. Finally, DNA-functionalized substrates were rinsed with Millipore H_2O, dried with N_2, and used immediately. For both SFG and SHG experiments, custom built Teflon cells (modified for flow capabilities in the case of SHG) were employed to mount the DNA-functionalized sample in the beamline.

To functionalize the 30 nm gold nanoparticles with a T_{40} sequence, the disulfide-terminated oligonucleotides were first cleaved with dithiothreitol (DTT) (0.1 M, 1 h) and purified on size exclusion columns (Sephadex G-10 DNA grade, GE Healthcare) following literature procedures.[55,56] The purified oligonucleotides were then added to the nanoparticles in water and slowly salted to 0.15 M NaCl over the course of 4 h. Sodium dodecyl sulfate (SDS, 0.01 wt %) was added to prevent the particles from sticking to the container. After sitting overnight, the particles were washed three times and then resuspended in aqueous solution (with or without Mg^{2+}).

2.3. Vibrational Sum Frequency Generation. Details of the table-top laser system used for all sum frequency generation experiments have been previously reported.[57−59] Briefly, the SFG layout includes a regeneratively amplified kHz Ti:Sapphire laser system (Spectra Physics Spitfire Pro, 2.5 mJ/pulse) producing 120 fs pulses having a wavelength of 800 nm. Half the beam is sent through a narrow-bandpass filter (F1.1-800.0-UNBLK-1.00, CVI Melles Griot) and used as the visible upconverter, while the other half pumps an optical parametric amplifier (Spectra Physics OPA-800CF) to produce a broadband infrared beam in the CH stretching frequency range (~3.4 μm, 140 cm^{-1} fwhm at 3 μm). The infrared and 800 nm upconverter beams are overlapped spatially and temporally at the sample interface at angles of 60 and 45° from normal, respectively. The SFG signal is spatially and spectrally isolated from the fundamental beams as well as other nonlinear processes and dispersed using a 0.5 m spectrograph (Acton Research) coupled to a liquid nitrogen-cooled, back-thinned charged coupled device (CCD) camera (Roper Scientific, 1340 × 100 $pixels^2$) for detection.

To probe the components of the vibrational modes that have a net orientation perpendicular to the interface we use the SSP-polarization combination, which indicates S-polarized SFG signal, S-polarized 800 nm light, and P-polarized IR light.[60,61] For each experiment, SFG spectra were recorded at the oligonucleotide-functionalized fused silica/aqueous solution interface with a total of five acquisitions per Mg^{2+} concentration, collected with a 5-min integration time, and averaged. The center frequency of the broadband IR pulse was optimized to detect the methyl, methylene, and methine modes of the thymine nucleobase (Figure 1a). All of the experiments described in this work were performed in triplicate, at pH 7, and using a salt concentration of 10 mM NaCl. All spectra were background-subtracted, calibrated to the 2850 and 3060 cm^{-1} peaks of polystyrene,[62−64] and normalized to the nonresonant sum frequency signal of a gold substrate.[60,65] To average spectra over multiple experiments, each set of spectra was normalized to the SFG intensity of the peak occurring at 2880 cm^{-1} prior to averaging.

2.4. Second Harmonic Generation. The laser and flow system used in all of the SHG $\chi^{(3)}$ experiments have been described extensively in our previous work.[54,66−69] Specifics of SHG experiments on oligonucleotide-functionalized fused silica surfaces are also available.[29,44,45,54] Briefly, SHG studies were performed using a kHz regeneratively amplified Ti:Sapphire laser (Spectra-Physics Hurricane, 120 fs pulse duration) pumping an optical parametric amplifier (OPA-

17340

dx.doi.org/10.1021/ja406551k | *J. Am. Chem. Soc.* 2013, 135, 17339−17348

Figure 1. (a) Chemical structure of a thymine nucleotide shown with methyl group highlighted in purple, and transition dipole moments of the symmetric (blue vector) and asymmetric (red vector) methylene modes. (b) Cartoon of surface-bound T_{40} in the extended conformation showing hypothesized alignment of methylene asymmetric stretches (red arrows). (c) Cartoon of surface-bound T_{40} in the collapsed conformation showing hypothesized cancelation of methylene asymmetric stretches (red arrows).

CF, Spectra-Physics). The incident beam was tuned, using the OPA, to a fundamental wavelength near 600 nm and the power was attenuated to 0.55 ± 0.05 μJ by directing it through a variable density filter. The p-polarized fundamental beam (ω) was focused onto the oligonucleotide-functionalized fused silica/water interface, where the second harmonic (2ω) is generated. A UV-grade Schott filter was used to filter out the fundamental beam. The second harmonic beam, collected without polarization selection, was directed through a monochromator set to 2ω and sent into photomultiplier tube, after which the detected signal was amplified and monitored using single photon counting techniques.

Descriptions of the flow setup and explanations of our adsorption/desorption ("on/off") traces are detailed in previous publications.[54,66−73] A flow rate of ~1 mL/s was maintained for all experiments presented herein. All of the experiments described in this work were performed at pH 7 and 10 mM NaCl for comparison to the SFG studies described above, to our previously published work on surface-bound single-stranded oligonucleotides, and to accommodate our modified Gouy−Chapman fitting equation. All adsorption isotherms presented in this work were recorded in triplicate.

2.5. Atomic Force Microscopy. The DNA-functionalized surfaces were imaged in fluid using a Bioscope II Scanning Probe Microscope with a NanoScope V controller (Digital Instruments) operating in tapping mode scanning 512 × 512 lines. A V-shaped SNL-10 probe (Veeco) with a 0.06 N/m spring constant and a 12−24 kHz resonant frequency was used. Images were initially taken in a 10 mM NaCl solution scanning a 1 μm square at 1−2 Hz. The scan size was then reduced to 333 nm with the scan rate remaining at 1−2 Hz. Images were taken for two or three different spots on the same sample. The 10 mM NaCl solution was then pipetted off of the surface and replaced with a 10 mM NaCl/3 mM $MgCl_2$ solution. The samples were then reimaged.

This experiment was carried out in triplicate on samples prepared separately in order to evaluate the uncertainties associated with our reported point estimates. All images were third-order flattened, low-pass filtered, and ranged from 0 to maximum height unless explicitly stated otherwise. Third-order flattening was employed to correct for the Z-offset between scan lines, the tilt of the image, and to remove artifact bowing due to piezo effects. The AFM images were loaded into an Igor Pro software program and converted into a matrix of height profiles for histogram analysis using 10 bins having a width of 1. Each histogram was comprised only from sample spots imaged on the same day with the same AFM tip in order to avoid variations in different AFM tips from affecting the height profiles.

2.6. SNA Gold Nanoparticle Hybridization Assay. T_{40} SNAs with 30 nm gold nanoparticle cores (70 pM) were placed in aqueous solutions of varied salt conditions consisting of (1) 150 mM NaCl with or without 3 mM Mg^{2+}, (2) 3 mM Mg^{2+} without NaCl, or (3) 10−16 mM NaCl without Mg^{2+}. The absorbance of these solutions at 535 nm

was monitored in cuvettes while stirring gently with magnetic stirbars. At t = 25 min, self-complementary hybridization linkers (5′-A_{20}-GCGC-3′, 1000-fold excess) were added to the SNA-AuNPs and their absorbance at 535 nm was monitored for three hours while maintaining constant temperature. A scheme of the hybridization assay is illustrated in Figure S1. Briefly, under conditions that favor hybridization, the introduction of the hybridization linker should result in the T_{40} SNA hybridizing to the A_{20} portion of the hybridization linker. The terminal GCGC portion of the hybridization linker is self-complementary, leading to the aggregation of multiple SNA-AuNPs conjugates. The close proximity of the gold nanoparticles in the hybridized SNA-AuNP conjugates redshifts their surface plasmon resonance, leading to changes in the absorbance at 535 nm upon hybridization.

The same experimental setup was employed in subsequent experiments for monitoring the melting temperature of hybridized SNA-AuNP conjugates prepared in the presence of 10 mM NaCl and $MgCl_2$ concentrations up to 10 mM. These experiments were carried out by monitoring the absorbance at 535 and 260 nm while ramping the cuvette temperature from 25 to 70 °C at a rate of 0.25 C/min.
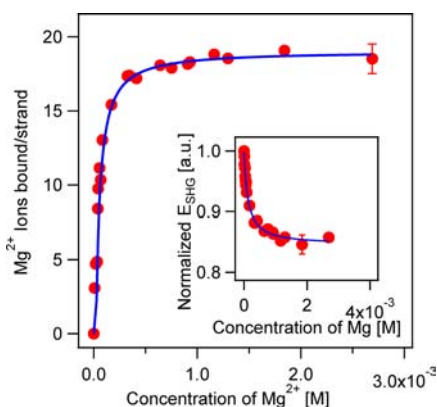
3. RESULTS AND DISCUSSION

3.1. Second Harmonic Generation: Quantifying Mg^{2+} Binding to Surface-Bound DNA. We have previously reported the binding of magnesium ions to surface-bound single-stranded DNA (ssDNA) for 20-mer sequences of the four natural nucleobases, and a similar approach is followed here.[29,54,74] The interaction of Mg^{2+} ions with the surface-bound T_{40} sequence was quantified by employing the $\chi^{(3)}$ technique, an off-resonant variant of second harmonic generation.[70,75−77] In the $\chi^{(3)}$ technique, the SHG response is modeled to be linearly dependent on the interfacial potential and has proven to be a valuable tool for studying the adsorption of ions to charged surfaces, such as single stranded oligonucleotides.[29,54] The details, advantages, and limitations of this technique, as well as its application to a variety of interfaces, are available in the literature.[70,75] Briefly, the second harmonic E-field (E_{SHG}), which is equal to the square root of the second harmonic intensity (I_{SHG}), is generated by the induced second-order polarization of the interface ($P_{2\omega}$) which can be defined as in eq 1. Here, A and B represent the product of the incident electric fields with the second- or third-order nonlinear susceptibility of the system, respectively, and are assumed to be constant over the range of study as supported by previously published sensitivity analyses.[70,78,79] Under these assumptions, the SHG E-field is directly related to the initial interfacial potential (Φ_0):

$$|E_{SHG}| = \sqrt{I_{SHG}} \propto P_{2\omega} = A + B\Phi_0 \qquad (1)$$

Surface-bound single-stranded T_{40} oligonucleotides produce a relatively high SHG E-field response if the negative charges on the phosphate backbone on the DNA produce a relatively high interfacial potential, i.e., under conditions of low ionic strength. When Mg^{2+} ions are introduced, the SHG E-field decreases if the divalent cations interact with the oligonucleotides such that the interfacial potential decreases, which may occur at the base or the phosphate sites. An example of such an interaction between Mg^{2+} ions and our T_{40}-mer is shown in the SHG $\chi^{(3)}$ isotherm (inset, Figure 2) which was produced by collecting Mg^{2+} adsorption/desorption traces in real time ("on/off traces") for a range of bulk Mg^{2+} concentrations (5×10^{-6} to 3×10^{-3} M) at pH 7 and in a 10 mM NaCl solution to maintain a relatively constant screening electrolyte concentration. The data were normalized by taking the square root of

Figure 2. Number of ions bound per T_{40} strand as a function of Mg^{2+} concentration calculated from SHG isotherm (inset).

the SHG intensity to obtain the SHG E-field at a given Mg^{2+} concentration and dividing it by the square root of the average SHG intensity obtained when the aqueous phase consists of just a 10 mM NaCl solution held at pH 7, i.e., before and after Mg^{2+} flow. The SHG E-field values were then plotted against the bulk Mg^{2+} concentration (inset, Figure 2). Previously published control studies verify that the resultant drop in the SHG E-field is not merely the result of increasing ionic strength but instead is due to divalent metal cation binding.[67] The isotherm was fit using the Langmuir modified Gouy−Chapman equation shown in eq 2.

$$E_{SHG} = A + B \sinh^{-1}\left[(\sigma_0 + \sigma_m)\left(\frac{K_{bind}[M]}{1 + K_{bind}[M]}\right)\right.$$
$$\left. \times \frac{30.19 \text{ M}^{1/2} \text{ m}^2 \text{ C}^{-1}}{\sqrt{C_{elec}}}\right] \quad (2)$$

Here, σ_0 is the initial surface charge density of the surface-bound oligonucleotide in the absence of Mg^{2+}, which was found to be -0.031 C/m^2 for 40-mer single strands,[44] σ_m is the maximum surface charge density due to bound Mg^{2+}, $[M]$ is the concentration of Mg^{2+} in bulk solution, C_{elec} is the total concentration of both screening electrolyte and analyte, K_{bind} is the observed binding constant of Mg^{2+} to DNA, and $30.19 \text{ M}^{1/2}$ m^2 C^{-1} is the product of the natural constants in the Gouy−Chapman equation. The error bars shown for the adsorption isotherm (inset, Figure 2) are reported to within a 95% confidence interval. The Gouy−Chapman theory was chosen over other mean field theories describing the electric double layer because it is applicable to the interfacial potential range covered here and avoids overparameterization.[29,54,80]

The Mg^{2+}-DNA binding constant, K_{bind}, was used to calculate the binding free energy, ΔG_{bind}, with reference to 55.5 M H$_2$O. For the T_{40}-mer, the K_{bind} was found to be $30(6) \times 10^3$ M^{-1}, yielding a ΔG_{bind} of Mg^{2+} to be $-35.0(2)$ kJ/mol, where the error is one standard deviation of the last digit (i.e., the error range is -34.8 to -35.2 kJ/mol). The uncertainty was calculated by propagating the error associated with K_{bind} (derived from the standard deviation of our fit of eq 2, plus an additional 5% to adjust for insensitivity to variations in the A and B parameters[70]) into the calculation of ΔG_{bind}. The disorder that is intrinsic to the system under investigation here means that it is difficult to define a plane of specific adsorption. We therefore emphasize that our analysis regarding the free energy of Mg^{2+} adsorption assumes only the work required to

move Mg^{2+} from the bulk to the diffuse plane. The ΔG_{bind} calculated here for a T_{40} sequence agrees with the ΔG_{bind} for a T_{21}-mer, which we recently reported to be $-35(1)$ kJ/mol.[29] This finding confirms our description of the free energy of binding as being an intrinsic property of a given nitrogenous base and analyte, i.e. it is independent of oligonucleotide length and number of binding sites.

The maximum Mg^{2+} ion loading per DNA strand was calculated from the surface charge density due to bound Mg^{2+} ions, σ_m, derived from our fit of eq 2 to the experimental adsorption isotherms. On the basis of our previously reported surface coverage of 5×10^{11} strands/cm^2 for immobilized oligonucleotides,[44] and our prior observation that magnesium ions bind as divalent ($+2$) species under the conditions presented here (10 mM background NaCl, pH 7),[54] the maximum Mg^{2+} loading at saturation was found to be 19(1) ions/strand. Thus, on average, all but 2 of the 40 negative charges from the phosphate backbone of the T_{40} sequence are neutralized upon binding of Mg^{2+}.

To calculate the Mg^{2+} ion density on the strands as a function of Mg^{2+} concentration in bulk aqueous solution, we rearranged eq 2 and accounted for oligonucleotide surface coverage to yield eq 3:
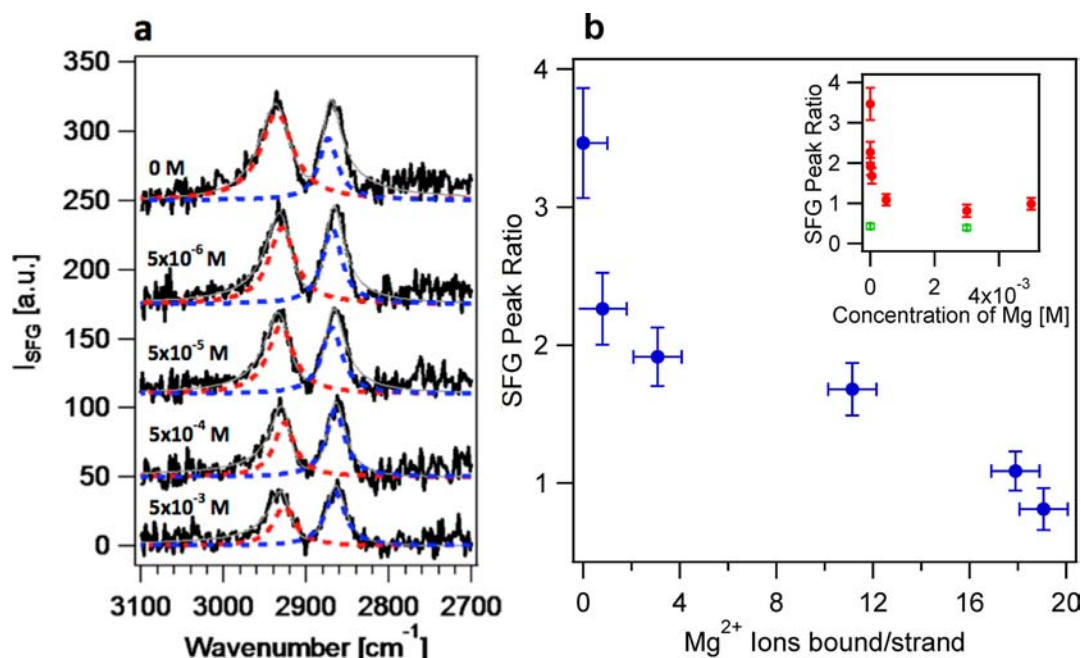
$$n_{ions} = \frac{N_A}{Fz\rho_{DNA}}\left(\left(\frac{\left(\sinh\left[\frac{E_{SHG} - A}{B}\right]\right)}{30.19 \text{ M}^{1/2} \text{ m}^2 \text{ C}^{-1}} \times \sqrt{C_{elec}}\right) - \sigma_0\right) \quad (3)$$

Here, N_A is Avogadro's number, F is Faraday's constant, z is the charge of magnesium ($+2$), and ρ_{DNA} is the surface coverage of T40 strands. The results are shown in Figure 2. The loading of Mg^{2+} on the T_{40} strands increases sharply at low Mg^{2+} concentrations until approximately 0.3 mM bulk concentration of Mg^{2+} ions, at which point it turns over and reaches full saturation of the 40-mer strands by 1 mM Mg^{2+}. To complement the second harmonic generation results that quantify the strength of interaction and the number of Mg^{2+} ions bound to DNA as we have shown here, we applied SFG and AFM in order to understand how specific binding of Mg^{2+} influences the structure and degree of order/disorder of the DNA strands.

3.2. Vibrational Sum Frequency Generation: Molecular Investigation of Surface-Bound DNA Structural Changes. Sum frequency generation provides exquisite sensitivity to changes in structure and orientation of surface species. There are many reports in the literature on the use of SFG to determine molecular orientation, characterize molecular structure, and analyze adsorption behavior.[63,81−93] Briefly, the intensity of the vibrational SFG signal (I_{SFG}) can be expressed as in eq 4,[94] where I_{Vis} and I_{IR} are the intensities of the incident beams, $\chi^{(2)}$ is the second-order nonlinear susceptibility, which is broken down into a resonant and nonresonant component ($\chi_{R_\nu}^{(2)}$ and $\chi_{NR}^{(2)}$, respectively), and γ_ν is the relative phase of the νth vibrational mode.

$$I_{SFG} \propto |\chi_{NR}^{(2)} + \sum_\nu |\chi_{R_\nu}^{(2)}|e^{i\gamma_\nu}|^2 I_{vis}I_{IR} \quad (4)$$

The resonant component of the SFG response depends on the number of adsorbates (N) and the molecular hyperpolarizability (β_ν) averaged over all orientations as shown in eq 5.

17342

dx.doi.org/10.1021/ja406551k | J. Am. Chem. Soc. 2013, 135, 17339−17348

Figure 3. (a) Average SFG spectra (black trace), spectral fits (gray line), and subpeaks (red and blue dotted lines indicating asymmetric and symmetric peaks, respectively) of surface-bound T_{40} ssDNA with increasing concentrations of Mg^{2+}, offset for clarity. (b) Correlation between SFG peak ratio, derived from spectral fits, and number of ions bound per strand as determined from SHG. Inset: SFG peak ratio as a function of Mg^{2+} concentration for T_{40} ssDNA (red dots) and NHS-linker (green dots, offset for clarity).

$$\chi_{R_{\nu}}^{(2)} \propto N\langle\beta_{\nu}\rangle \propto \frac{A_K M_{IJ}}{\omega_{\nu} - \omega_{IR} - i\Gamma_{\nu}} \qquad (5)$$
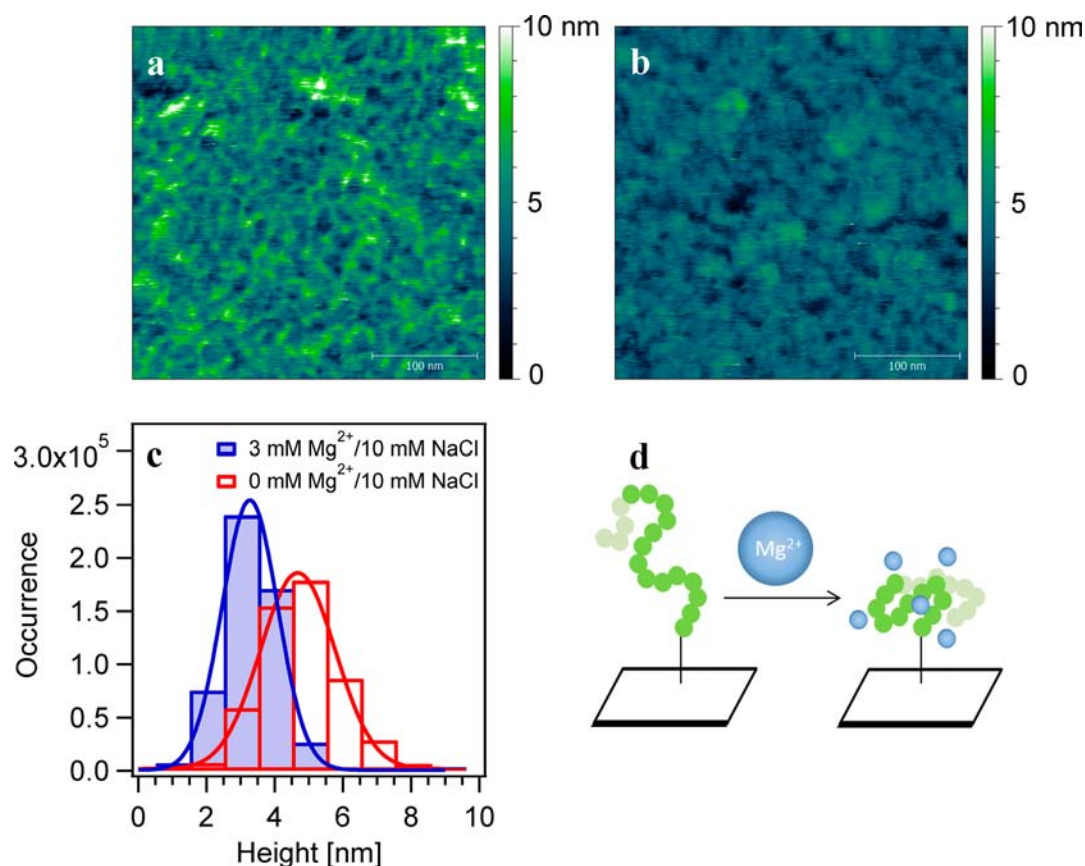
Equation 5 enables the analysis of surface structure and orientation without the use of labels since a large signal enhancement occurs when the incident IR frequency (ω_{IR}) is resonant with a sum frequency active vibrational mode (ω_{ν}). As shown here, SFG-allowed modes must be both IR and Raman active, where A_K is the IR transition moment, M_{IJ} is the Raman transition probability, and Γ_{ν} is the natural line width of the transition.

The T_{40} sequence length studied here provides a substantial number of oscillators without sacrificing DNA synthesis yield or accruing undue cost. Here, SFG was used to study the structure of T_{40} single-stranded sequences under the same conditions used for SHG experiments. In a static cell, T_{40}–functionalized silica windows were exposed to increasing concentrations of Mg^{2+} (ranging from 5×10^{-6} to 5×10^{-3} M Mg^{2+}) with a background salt concentration of 10 mM NaCl at pH 7. The resulting spectra are shown in Figure 3a, as an average of two or more experiments, for representative Mg^{2+} concentrations. The spectra are composed of two peaks centered at 2930 and 2868 cm^{-1} that are due to the oscillators on the organic linker that is used to covalently attach DNA to the surface (Figure S2) and the methylene and methine modes from the ribose sugar, provided those modes are associated with a net orientation as opposed to being randomly oriented, in which case the SFG signal should vanish. Spectral peaks attributable to the methyl groups on the thymine nucleobases, of which there are forty per strand studied here, are not observed in Figure 3a, indicating that the methyl groups along the T40-mer single strands are highly disordered. Note that we recently reported[42,43] that the CH_3 groups of thymine oligonucleotides do yield SFG signal if they are duplexed to their adenine counterparts, with signal contributions at 2960 and 2880 cm^{-1} for the asymmetric and

symmetric methyl stretches, respectively. The aromatic groups are not observed under any molecular arrangement studied thus far with our experimental setup.

Spectral fits were obtained by using a custom-written Igor Pro software procedure that convolutes Lorentzian peaks and a nonresonant background as detailed previously.[57,65] Overlapping Lorentzian peaks were allowed to interfere with each other with fixed 0° or 180° phases; the sign of the amplitude can be negative or positive to account for this phase.[60,65,95] Spectra were fit to two modes, one above and one below 2900 cm^{-1} (hereafter referred to as the asymmetric and symmetric peaks, respectively), and subsequently, the ratios between the two peak amplitudes were analyzed as a function of magnesium concentration. For spectral fitting, we assume that the peaks in the symmetric region below 2900 cm^{-1} are decoupled from the asymmetric region above 2900 cm^{-1}, and that the majority of the signal is due to methylene stretching modes along the DNA strand and linker. Initial fit parameters were input into the program and best fits were selected based on fit convergence and minimization of the standard deviation of all coefficients. The asymmetric and symmetric subpeaks (red and blue dotted lines, respectively) from each spectral fit (thin gray line) are shown in Figure 3a, and a table of the fit parameters can be found in the Supporting Information (Table S1). After fitting the spectra, individual peak amplitudes were multiplied by their respective Γ_{ν} values to account for variations in the natural line width between fits, and the ratio between the asymmetric to symmetric peak amplitude was taken.

The inset in Figure 3b plots the asymmetric to symmetric peak amplitude ratio as a function of magnesium concentration. The data reveals a distinct drop in the SFG peak intensity ratio for the T_{40}-mers as magnesium is added and corresponds well with the SHG results. Changes in the SFG signal intensities could be indicative of structural reordering of the oligonucleotides, as evidenced by the fact that the ratio for the NHS-linker

Figure 4. AFM images of T_{40} ssDNA (a) under 0 mM Mg^{2+}/10 mM NaCl and (b) under 3 mM Mg^{2+}/10 mM NaCl. (c) Histogram analysis of T_{40} ssDNA images with and without Mg^{2+}. (d) Cartoon depiction of possible structural reordering and collapse.

remains constant over the same range of magnesium concentrations (inset, Figure 3b) — an observation that is also supported by the results from our AFM studies (*vide infra*).

A plot of the SFG peak ratio versus the average number of Mg^{2+} ions bound per DNA strand illustrates the correlation of the drop in SFG peak ratio with increasing Mg^{2+} binding (Figure 3b). The SFG spectral changes are complete when T_{40} is saturated with Mg^{2+} ions, as identified by SHG at bulk concentrations around 1 mM Mg^{2+} (corresponding to 18−20 Mg^{2+} ions bound, *vide supra*). One possible explanation for this observation, which is also corroborated by our AFM experiments revealing a *ca.* 30% length contraction of the oligonucleotides upon Mg^{2+} binding (Figure 4, *vide infra*), is that the DNA strands are originally extended out from the surface in the absence of Mg^{2+} ions, and adopt a collapsed structure once the metal ions bind.[96] Figure 1 shows the transition dipole moments of the asymmetric and the symmetric methylene stretches in thymine. The SFG spectra discussed here are due to the coherent addition of these oscillators, which will change as the DNA organization changes in the presence of Mg^{2+}.

The findings presented here are consistent with the notion that the Coulombic repulsions between the nucleotides force the single-stranded sequence to straighten out into the bulk in the absence of Mg^{2+}. In this case, the asymmetric stretches of the methylene groups of the ribose sugars are likely to be aligned along the probe direction of the SFG experiment (perpendicular to the surface) if the strands extend into the bulk (Figure 1b), yielding higher SSP-polarized SFG intensity

in the methylene asymmetric stretching mode. Upon Mg^{2+} binding, the DNA strand should collapse due to the decreased Coulombic repulsions between the nucleobases. This Coulomb collapse may lead to the formation of a random coil structure in which the molecular orientation distribution of the DNA methylene groups becomes randomized (Figure 1c). This effect should be evidenced by a decrease in the SFG peak intensity of the asymmetric stretching mode, which is indeed observed. As we show in the Supporting Information, the SFG intensity in the symmetric stretching region is probably dominated by the CH stretches of the underlying linker and, therefore, is likely to remain constant throughout the experiment. In fact, in a case where the NHS-linker yielded little asymmetric CH stretching intensity (Figure S2a), the spectral changes in the asymmetric CH stretching region due to DNA collapse are much more pronounced (Figure S2b). To further test structural reordering of T_{40}-mers upon Mg^{2+} binding, we employ AFM imaging to quantify possible height changes.

3.3. Atomic Force Microscopy: Imaging DNA Height Profiles upon Mg^{2+} Binding. AFM images of T_{40} functionalized surfaces with and without Mg^{2+} ions present were taken and analyzed under aqueous solution as described in the Experimental Methods section. Solutions of 3 mM Mg^{2+} were used for AFM analysis since this concentration was well within the saturation regime of 19(1) bound Mg^{2+} ions per strand from the SHG analysis (*vide supra*). Representative AFM tapping mode images of the T_{40} surfaces are substantially brighter in the absence vs the presence of Mg^{2+} (Figure 4a,b). The height histogram analysis of the images shown (Figure 4c) indicates an average height of 4.68(3) nm for the T_{40} strands

over the linker-functionalized fused silica surface without Mg^{2+}; however, the height decreases to 3.272(3) nm in the presence of 3 mM Mg^{2+}. As mentioned in the previous section, this 30% decrease in the measured height profile supports the SFG analysis in which the surface-bound DNA collapses or coils with the decrease in Coulombic repulsions from binding Mg^{2+}, as depicted in Figure 4d.

We note that the absolute height measured by AFM is not indicative of the DNA length since all images are scaled such that the global minimum of the imaged surface is defined as the zero point. The global minimum may vary based on substrate defects; thus, we only compared AFM images with and without Mg^{2+} via histogram analysis when they were measured on the same substrate with the same AFM tip. While the exact height profiles may vary between substrates and days, the trends observed upon binding Mg^{2+} were the same and are compiled as average percentage changes in Table 1. On average, the DNA height profile drops by 26.9(1)% after binding Mg^{2+}.

Table 1. Average Changes in AFM Height Profile

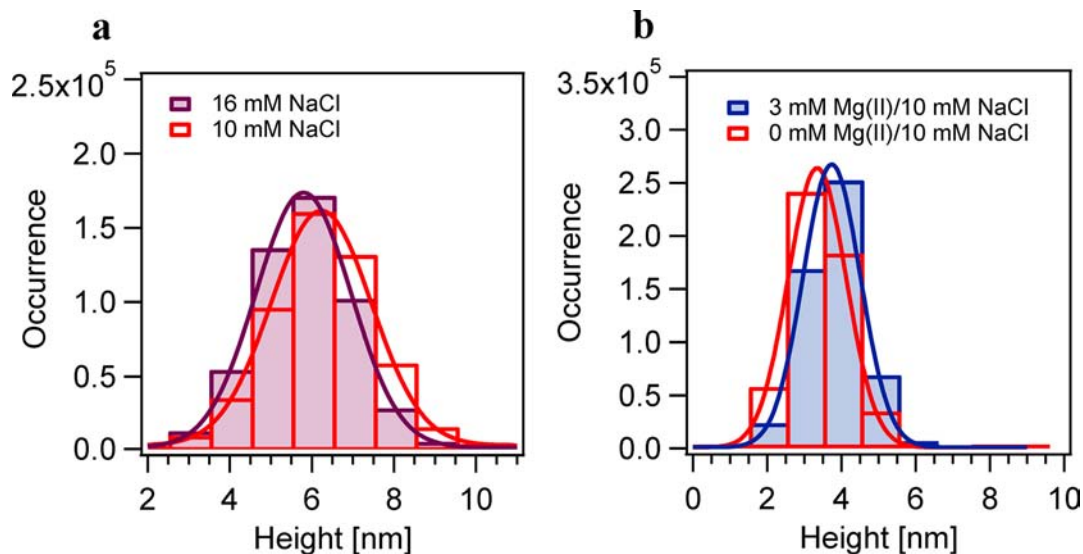| surface	aqueous interface		average % height change
	initial	final	
T_{40} ssDNA	10 mM NaCl	3 mM Mg 10 mM NaCl	−26.9(1)
T_{40} ssDNA	10 mM NaCl	16 mM NaCl	−8.84(4)
NHS-linker	10 mM NaCl	3 mM Mg 10 mM NaCl	+10.33(2)

Control experiments confirmed that the structural reordering was dependent on Mg^{2+} binding to DNA (Figure 5), as opposed to changes in ionic strength. In these controls, we analyzed the response of T_{40} functionalized substrates to a sodium chloride solution with an equal ionic strength (16 mM NaCl) to the magnesium concentration used. Figure 5a shows the histogram analysis carried out for the ionic strength control, in which only an 8.84(4)% decrease in height was observed on average. While we expect that increasing the bulk ionic strength will contribute to the charge screening, the much less pronounced contraction in length observed in this control

experiment indicates that much of the structural reordering of surface-bound T_{40} is indeed dependent on Mg^{2+}, which has a reasonably strong free energy of binding (−35.5(5) kJ/mol) as determined by the SHG measurements discussed above. An additional control study shows that the height profile of the hydrolyzed NHS-linker, in the absence of surface-bound DNA (Figure 5b), increases slightly by 10.33(2)% with the addition of Mg^{2+}, which is consistent with published SHG results showing that the NHS-linker is not affected by salt concentrations in the regime of interest.[45] We conclude that the structural changes observed in Figures 3 and 4 are largely due to Mg^{2+} binding to the DNA strands and that structural changes attributable to the organic linker or increases in ionic strength by NaCl are minor.

Dynamic light scattering (DLS) measurements were also carried out on T_{40}-functionalized 30 nm gold nanoparticles in the presence of 0, 1, 2.5, and 8 mM Mg^{2+} solutions (Figure S4) to verify that a similar trend of DNA strand collapse occurs for the colloid system used in the hybridization assay. DLS results indicate that the hydrodynamic radius of the T_{40}-gold nanoparticles does indeed contract in the presence of magnesium ions by roughly 20%.
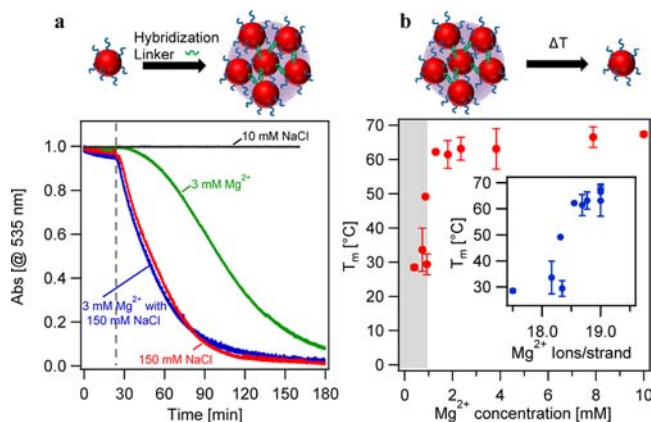
3.4. SNA Gold Nanoparticle Hybridization Assay: Impact of Mg^{2+} Binding on DNA Hybridization and Duplex Stability. To address the question of how Mg^{2+} binding and the collapse of the oligonucleotide structure might impact the hybridization of target and capture strands in a sensor-type application, we developed an assay to track surface-bound DNA hybridization under varying electrolyte conditions. As described in the Experimental Methods section, the plasmon resonance of 30 nm gold nanoparticles (AuNP) functionalized with a thiol-modified T_{40} sequence (SNA-AuNP) was tracked via UV−vis spectroscopy after the introduction of a self-complementary hybridization linker (5′-A_{20}-GCGC-3′). The relatively large gold nanoparticles (30 nm) were chosen to avoid effects of curvature and best mimic a flat surface.[89] Under the proper conditions, the hybridization linker is expected to partially hybridize with the T_{40} ssDNA on the AuNPs, leaving a sticky end that is free to hybridize with

Figure 5. AFM histogram analysis of (a) T_{40} ssDNA with 16 mM NaCl control and (b) hydrolyzed NHS-linker, without DNA, in the absence and presence of Mg^{2+}.

another linker, thereby directing particle aggregation and red shifting the electronic absorbance away from 535 nm.[16]

As shown in Figure 6a, the absorbance at 535 nm decreases as hybridization occurs for experiments carried out in solutions

Figure 6. SNA-functionalized gold nanoparticle hybridization assay and melting temperature transitions tracked by UV–vis spectroscopy. (a) Hybridization tracked in the presence and absence of magnesium at various ionic strengths. A shift in the absorbance wavelength is monitored as 30 nm gold nanoparticles, functionalized with thiol modified-T_{40} ssDNA, aggregate when the complementary linker is added (indicated by dashed gray line). All data were normalized to 1 and referenced to 0 for direct comparison. Hybridization proceeds in the presence of 150 mM NaCl (red trace), 3 mM Mg^{2+}/150 mM NaCl (blue trace), and 3 mM Mg^{2+} (green trace), but does not in 10 mM NaCl (black trace). (b) DNA melting temperatures tracked as a function of magnesium concentration, ranging from 0.4 mM − 10 mM Mg^{2+} with 10 mM background NaCl. Gray shading indicates region of low duplex stability. (Inset) DNA melting temperature as a function the average number of Mg^{2+} ions bound (calculated from SHG). Please see text for details.

containing 150 mM NaCl (red trace), 3 mM Mg^{2+}/150 mM NaCl (blue trace), and 3 mM Mg^{2+} (green trace). However, the absorbance remains constant for solutions of 10 mM NaCl (no Mg^{2+} present, black trace), indicating that hybridization does not occur over the timespan we investigated at low ionic strengths without Mg^{2+}. Clearly, Mg^{2+} binding is necessary to drive hybridization at low ionic strengths, even in the absence of NaCl. We note that Figure 6a is representative of all trials, which are shown in the Supporting Information (Figures S5– S7), and our results are in agreement with related reports on the shielding effect of magnesium cations on surface-bound DNA hybridization.[97] We also note that there is little discernible difference between the hybridization rate at higher ionic strengths with and without Mg^{2+} present. When compared to solutions containing higher ionic strengths (i.e., 150 mM NaCl and 3 mM Mg^{2+}/150 mM NaCl), the slower kinetics observed for the 3 mM Mg^{2+} solution are likely due to the higher electrostatic repulsion experienced between DNA strands at the lower ionic strength solution, the collapsed structure of DNA in the presence of magnesium cations, or other processes hindering hybridization.

To investigate how duplex stability depends on magnesium concentration, melting temperatures (T_m) of the hybridized SNA-AuNPs were monitored as a function of magnesium concentration (Figure 6b). Magnesium concentrations were varied from 0.4 to 10 mM Mg^{2+} while a constant background concentration of 10 mM NaCl was maintained for all T_m

experiments (no hybridization was observed below 0.4 mM Mg^{2+}/10 mM NaCl). Figure 6b illustrates the sharp increase in the DNA melting temperature that occurs around 1−2 mM Mg^{2+}, which coincides with the saturation regime discussed above in sections 3.1 and 3.2. When the T_{40} sequence is not fully saturated with Mg^{2+} ions, i.e., below 1 mM Mg^{2+}, the average T_m is 31(3)°C, indicating low duplex stability (Figure 6b, gray shaded region). Above the point of Mg^{2+} saturation, the T_m increases dramatically, doubling to an average of 64(2)°C. Plotting T_m versus the average number of Mg^{2+} ions bound per T_{40} sequence (inset, Figure 6b) illustrates that average Mg^{2+} loadings between 17.5 and 18.3 Mg^{2+} ions/strand result in low duplex melting temperatures. The melting temperature then suddenly doubles over a very narrow range of Mg^{2+} strand loadings, at an average of 18.3−18.8 Mg^{2+} ions/ strand.

We note that our previous SHG studies[29,74] reported that a single A_{21} strand can bind three Mg^{2+} ions, while guanine and cytosine can bind eleven Mg^{2+} ions per 21-mer. Thus, we expect that the hybridization linker will also interact to some degree with magnesium ions present in solution.

The quantitative parameters obtained using the label-free multipronged approach presented here may allow for metal– DNA interactions as well as DNA target–capture interactions in biosensor platforms under ionic strength conditions that would otherwise not be feasible. In fact, our SNA-AuNP assay shows that hybridization is unfavorable at low ionic strengths if NaCl is the only electrolyte present, but that hybridization becomes favorable at low ionic strengths and in the absence of NaCl when 3 mM Mg^{2+} is introduced, although slower kinetics are observed. We find that the addition of just one Mg^{2+} ion to an almost charged-neutralized T_{40} strand on SNA-containing gold metal nanoparticles substantially increases the stability of the duplexes formed from them, as evidenced by a doubling of their T_m values. Moreover, our findings are consistent with a charge titration effect in which the electrostatic barrier to DNA duplex stability is not removed until 95% of all the charges on the DNA backbone are neutralized. The investigation of this effect revealed that (1) hybridization does not occur if an average of 17.5 or less Mg^{2+} ions are bound per T_{40} strand, which is not reached until the Mg^{2+} concentration approaches 0.5 mM; (2) hybridization proceeds, albeit with low duplex stability having an average T_m of 31(3)°C, if an average of 17.5−18.0 Mg^{2+} ions are bound; and (3) highly stable duplexes having a T_m of 64(2)°C form if 18.5−19.0 Mg^{2+} ions are bound, corresponding to saturation of the T_{40} strand.

The consequences of our findings are as follows: when operating under low ionic strength conditions, the addition of just 2 mM Mg^{2+} is sufficient to promote stable DNA−DNA interactions for a surface-bound T_{40} sequence. Enhanced duplex stability and hybridization efficiency is observed when the DNA strands are saturated with Mg^{2+} ions, which may vary with DNA sequence composition. Thus, if metal ion strand saturation is known for a particular DNA sequence, one may be able to predict the stability enhancement of the duplex in the presence of magnesium. Our previous work has reported the free energy of Mg^{2+}−DNA binding and the number of Mg^{2+} ions bound/strand at saturation for a number of different DNA sequences,[29,54,74] which can now be applied to optimizing Mg^{2+} concentrations for alternative sequences. These results are likely extendable to other divalent as well as trivalent metal cations with preference toward the phosphate sites.

17346

dx.doi.org/10.1021/ja406551k | *J. Am. Chem. Soc.* 2013, 135, 17339−17348

4. CONCLUSIONS

In conclusion, we have reported a series of label-free independent experiments carried out under identical aqueous phase conditions that quantify the number of Mg^{2+} ions binding to surface-bound T_{40} sequences, the subsequent reordering of the DNA on the surface at submillimolar magnesium concentrations and above, and the consequences of Mg^{2+} binding for DNA−DNA interactions. The data indicate that, within error, 18−20 Mg^{2+} ions are bound to the T_{40} strand at saturation and that the metal−DNA interaction is associated with a near 30% length contraction of the strand. Strand collapse is complete when Mg^{2+} begins to saturate the DNA strands after an average of 18.3 Mg^{2+} ions are bound per strand. Such structural reordering is attributed to increased charge screening as the Mg^{2+} ions bind to the negatively charged DNA, reducing repulsive Coulomb forces between nucleotides and allowing the ssDNA to collapse or coil upon itself. The preinteraction behavior between Mg^{2+} ions and surface bound single-stranded DNA influences hybridization efficiency in the absence of NaCl, and enhances duplex stability. The melting temperature of DNA duplexes was increased dramatically in the presence of just 2 mM Mg^{2+}, corresponding to the saturation regime of Mg^{2+} binding to surface-bound T_{40} strands.

The label-free and quantitative parameters obtained using the multipronged approach discussed here may allow for the tailoring of metal-DNA interactions, as well as DNA target−capture interactions in relevant biosensor platforms and DNA modeling studies. An important implication of the results presented here is that the presence of magnesium ions in a system will sufficiently stabilize DNA duplexes to allow DNA-based separation, extraction, and detection processes to proceed at low ionic strength. Future work should address the effect of oligomer length on cation strand loading and structural reordering. Work with additional DNA sequences should address the generalizability of these results. Additionally, future SFG and AFM experiments should address the role reversibility plays in strand height and orientation.

◼ ASSOCIATED CONTENT

Ⓢ Supporting Information

SFG spectra of the organic NHS linker, spectral fits and fitting parameters, and hybridization experiments. This material is available free of charge via the Internet at http://pubs.acs.org.

◼ AUTHOR INFORMATION

Corresponding Author
geigerf@chem.northwestern.edu
Notes
The authors declare no competing financial interest.

◼ ACKNOWLEDGMENTS

◼ REFERENCES

(1) Fodor, S. P. A. *Science* **1997**, *277*, 393.
(2) Chee, M.; Yang, R.; Hubbell, E.; Berno, A.; Huang, X. C.; Stern, D.; Winkler, J.; Lockhart, D. J.; Morris, M. S.; Fodor, S. P. A. *Science* **1996**, *274*, 610.
(3) Stoughton, R. B. *Annu. Rev. Biochem.* **2005**, *74*, 53.
(4) Lockhart, D. J.; Winzeler, E. A. *Nature* **2000**, *405*, 827.
(5) Shuber, A. P.; Michalowsky, L. A.; Scott Nass, G.; Skoletsky, J.; Hire, L. M.; Kotsopoulos, S. K.; Phipps, M. F.; Barberio, D. M.; Klinger, K. W. *Hum. Mol. Genet.* **1997**, *6*, 337.
(6) Tam, J. M.; Song, L.; Walt, D. R. *Biosens. Bioelectron.* **2009**, *24*, 2488.
(7) Heller, M. J. *Annu. Rev. Biomed. Eng.* **2002**, *4*, 129.
(8) Hornes, E.; Korsnes, L. *Gene Anal. Tech.* **1990**, *7*, 145.
(9) Jacobsen, N.; Nielsen, P. S.; Jeffares, D. C.; Eriksen, J.; Ohlsson, H.; Arctander, P.; Kauppinen, S. *Nucleic Acids Res.* **2004**, *32*, No. e64.
(10) Seferos, D. S.; Giljohann, D. A.; Hill, H. D.; Prigodich, A. E.; Mirkin, C. A. *J. Am. Chem. Soc.* **2007**, *129*, 15477.
(11) Rosi, N. L.; Giljohann, D. A.; Thaxton, C. S.; Lytton-Jean, A. K. R.; Han, M. S.; Mirkin, C. A. *Science* **2006**, *312*, 1027.
(12) Bielinska, A.; KukowskaLatallo, J. F.; Johnson, J.; Tomalia, D. A.; Baker, J. R. *Nucleic Acids Res.* **1996**, *24*, 2176.
(13) Liu, W.; Zhong, H.; Wang, R.; Seeman, N. C. *Angew. Chem., Int. Ed.* **2011**, *50*, 264.
(14) Seeman, N. C. *Nature* **2003**, *421*, 427.
(15) Park, S. Y.; Lytton-Jean, A. K. R.; Lee, B.; Weigand, S.; Schatz, G. C.; Mirkin, C. A. *Nature* **2008**, *451*, 553.
(16) Mirkin, C. A.; Letsinger, R. L.; Mucic, R. C.; Storhoff, J. J. *Nature* **1996**, *382*, 607.
(17) Alivisatos, A. P.; Johnson, K. P. *Nature* **1996**, *382*, 609.
(18) Macfarlane, R. J.; Jones, M. R.; Senesi, A. J.; Young, K. L.; Lee, B.; Wu, J.; Mirkin, C. A. *Angew. Chem., Int. Ed.* **2010**, *49*, 4589.
(19) Macfarlane, R. J.; Lee, B.; Jones, M. R.; Harris, N.; Schatz, G. C.; Mirkin, C. A. *Science* **2011**, *334*, 204.
(20) Wolf, F. I.; Cittadini, A. *Mol. Aspects Med.* **2003**, *24*, 3.
(21) Henegariu, O.; Heerema, N. A.; Dlouhy, S. R.; Vance, G. H.; Vogt, P. H. *BioTechniques* **1997**, *23*, 504.
(22) Ignatov, K. B.; Miroshnikov, A. I.; Kramarov, V. M. *Russ. J. Bioorg. Chem.* **2003**, *29*, 368.
(23) von Ahsen, N.; Wittwer, C. T.; Schütz, E. *Clin. Chem.* **2001**, *47*, 1956.
(24) Zubay, G. *Biochim. Biophys. Acta* **1959**, *32*, 233.
(25) Chiu, T. K.; Dickerson, R. E. *J. Mol. Biol.* **2000**, *301*, 915.
(26) Hackl, E. V.; Kornilova, S. V.; Kapinos, L. E.; Andrushchenko, V. V.; Galkin, V. L.; Grigoriev, D. N.; Blagoi, Y. P. *J. Mol. Struct.* **1997**, *408−409*, 229.
(27) Duguid, J.; Bloomfield, V. A.; Benevides, J.; Thomas, G. J., Jr. *Biophys. J.* **1993**, *65*, 1916.
(28) Anastassopoulou, J.; Theophanides, T. *Crit. Rev. Oncol. Hematol.* **2002**, *42*, 79.
(29) Holland, J. G.; Malin, J. N.; Jordan, D. S.; Morales, E.; Geiger, F. M. *J. Am. Chem. Soc.* **2011**, *133*, 2567.
(30) Misra, V. K.; Draper, D. E. *Biopolymers* **1998**, *48*, 113.
(31) Ott, G. S.; Ziegler, R.; Bauer, W. R. *Biochemistry* **1975**, *14*, 3431.
(32) Owczarzy, R.; Moreira, B. G.; You, Y.; Behlke, M. A.; Walder, J. A. *Biochemistry* **2008**, *47*, 5336.
(33) Record, M. T. *Biopolymers* **1975**, *14*, 2137.
(34) Blagoi, Y. P.; Sorokin, V. A.; Valeyev, V. A.; Khomenko, S. A.; Gladchenko, G. O. *Biopolymers* **1978**, *17*, 1103.

(35) Eichhorn, G. L.; Shin, Y. A. *J. Am. Chem. Soc.* **1968**, *90*, 7323.

(36) Williams, A. P.; Longfellow, C. E.; Freier, S. M.; Kierzek, R.; Turner, D. H. *Biochemistry* **1989**, *28*, 4283.

(37) Cutler, J. I.; Auyeung, E.; Mirkin, C. A. *J. Am. Chem. Soc.* **2012**, *134*, 1376.

(38) Seferos, D. S.; Prigodich, A. E.; Giljohann, D. A.; Patel, P. C.; Mirkin, C. A. *Nano Lett.* **2008**, *9*, 308.

(39) Voet, D.; Voet, J. G. *Biochemistry*, 3rd ed.; Wiley Text Books: New York, NY, 2004.

(40) Asanuma, H.; Noguchi, H.; Uosaki, K.; Yu, H.-Z. *J. Am. Chem. Soc.* **2008**, *130*, 8016.

(41) Howell, C.; Schmidt, R.; Kurz, V.; Koelsch, P. *Biointerphases* **2008**, *3*, FC47.

(42) Walter, S. R.; Geiger, F. M. *J. Phys. Chem. Lett.* **2010**, *1*, 9.

(43) Stokes, G. Y.; Gibbs-Davis, J. M.; Boman, F. C.; Stepp, B. R.; Condie, A. G.; Nguyen, S. T.; Geiger, F. M. *J. Am. Chem. Soc.* **2007**, *129*, 7492.

(44) Boman, F. C.; Gibbs-Davis, J. M.; Heckman, L. M.; Stepp, B. R.; Nguyen, S. T.; Geiger, F. M. *J. Am. Chem. Soc.* **2009**, *131*, 844.

(45) Boman, F. C.; Musorrafiti, M. J.; Gibbs, J. M.; Stepp, B. R.; Salazar, A. M.; Nguyen, S. B. T.; Geiger, F. M. *J. Am. Chem. Soc.* **2005**, *127*, 15368.

(46) Casero, E.; Darder, M.; Díaz, D. J.; Pariente, F.; Martín-Gago, J. A.; Abruña, H.; Lorenzo, E. *Langmuir* **2003**, *19*, 6230.

(47) Costa, L. T.; Kerkmann, M.; Hartmann, G.; Endres, S.; Bisch, P. M.; Heckl, W. M.; Thalhammer, S. *Biochem. Biophys. Res. Commun.* **2004**, *313*, 1065.

(48) Humeník, D.; Chorvát, D., Jr.; Novotný, I.; Tvarožek, V.; Oretskaya, T. S.; Hianik, T. *Med. Eng. Phys.* **2006**, *28*, 956.

(49) Longo, G.; Girasole, M.; Pompeo, G.; Cricenti, A.; Andreano, G.; Cattaruzza, F.; Cellai, L.; Flamini, A.; Guarino, C.; Prosperi, T. *Biomol. Eng.* **2007**, *24*, 53.

(50) Wu, N.; Zhou, X.; Czajkowsky, D. M.; Ye, M.; Zeng, D.; Fu, Y.; Fan, C.; Hu, J.; Li, B. *Nanoscale* **2011**, *3*, 2481.

(51) Hansma, H. G.; Laney, D. E.; Bezanilla, M.; Sinsheimer, R. L.; Hansma, P. K. *Biophys. J.* **1995**, *68*, 1672.

(52) Putman, C. A. J.; Van der Werf, K. O.; De Grooth, B. G.; Van Hulst, N. F.; Greve, J. *Appl. Phys. Lett.* **1994**, *64*, 2454.

(53) Shlyakhtenko, L. S.; Gall, A. A.; Weimer, J. J.; Hawn, D. D.; Lyubchenko, Y. L. *Biophys. J.* **1999**, *77*, 568.

(54) Holland, J. G.; Jordan, D. S.; Geiger, F. M. *J. Phys. Chem. B* **2011**, *115*, 8338.

(55) Hill, H. D.; Mirkin, C. A. *Nat. Protoc.* **2006**, *1*, 324.

(56) Hurst, S. J.; Lytton-Jean, A. K. R.; Mirkin, C. A. *Anal. Chem.* **2006**, *78*, 8313.

(57) Hayes, P. L.; Chen, E. H.; Achtyl, J. L.; Geiger, F. M. *J. Phys. Chem. A* **2009**, *113*, 4269.

(58) Stokes, G. Y.; Buchbinder, A. M.; Gibbs-Davis, J. M.; Scheidt, K. A.; Geiger, F. M. *J. Phys. Chem. A* **2008**, *112*, 11688.

(59) Stokes, G. Y.; Buchbinder, A. M.; Gibbs-Davis, J. M.; Scheidt, K. A.; Geiger, F. M. *Vib. Spectrosc.* **2009**, *50*, 86.

(60) Esenturk, O.; Walker, R. A. *J. Phys. Chem. B* **2004**, *108*, 10631.

(61) Lü, R.; Gan, W.; Wang, H. *Chin. Sci. Bull.* **2003**, *48*, 2183.

(62) Ding, F.; Zhong, Q.; Brindza, M. R.; Fourkas, J. T.; Walker, R. A. *Opt. Express* **2009**, *17*, 14665.

(63) Buchbinder, A. M.; Weitz, E.; Geiger, F. M. *J. Am. Chem. Soc.* **2010**, *132*, 14661.

(64) Esenturk, O.; Walker, R. A. *J. Chem. Phys.* **2006**, *125*, 174701.

(65) Buchbinder, A. M.; Weitz, E.; Geiger, F. M. *J. Phys. Chem. C* **2009**, *114*, 554.

(66) Hayes, P. L.; Malin, J. N.; Konek, C. T.; Geiger, F. M. *J. Phys. Chem. A* **2008**, *112*, 660.

(67) Malin, J. N.; Hayes, P. L.; Geiger, F. M. *J. Phys. Chem. C* **2009**, *113*, 2041.

(68) Hayes, P. L.; Gibbs-Davis, J. M.; Musorrafiti, M. J.; Mifflin, A. L.; Scheidt, K. A.; Geiger, F. M. *J. Phys. Chem. C* **2007**, *111*, 8796.

(69) Mifflin, A. L.; Musorrafiti, M. J.; Konek, C. T.; Geiger, F. M. *J. Phys. Chem. B* **2005**, *109*, 24386.

(70) Hayes, P. L.; Malin, J. N.; Jordan, D. S.; Geiger, F. M. *Chem. Phys. Lett.* **2010**, *499*, 183.

(71) Malin, J. N.; Geiger, F. M. *J. Phys. Chem. A* **2010**, *114*, 1797.

(72) Malin, J. N.; Holland, J. G.; Geiger, F. M. *J. Phys. Chem. C* **2009**, *113*, 17795.

(73) Al-Abadleh, H. A.; Voges, A. B.; Bertin, P. A.; Nguyen; Geiger, F. M. *J. Am. Chem. Soc.* **2004**, *126*, 11126.

(74) Holland, J. G.; Geiger, F. M. *J. Phys. Chem. B* **2012**, *116*, 6302.

(75) Eisenthal, K. B. *Chem. Rev.* **1996**, *96*, 1343.

(76) Xiao, X.-D.; Vogel, V.; Shen, Y. R. *Chem. Phys. Lett.* **1989**, *163*, 555.

(77) Zhao, X.; Subrahmanyan, S.; Eisenthal, K. B. *Chem. Phys. Lett.* **1990**, *171*, 558.

(78) Jordan, D. S.; Malin, J. N.; Geiger, F. M. *Environ. Sci. Technol.* **2010**, *44*, 5862.

(79) Jena, K. C.; Covert, P. A.; Hore, D. K. *J. Phys. Chem. Lett.* **2011**, *2*, 1056.

(80) Stumm, W.; Morgan, J. J. *Aquatic Chemistry*, 3rd ed.; John Wiley & Sons, Inc.: New York, 1996.

(81) Casillas-Ituarte, N. N.; Chen, X. K.; Castada, H.; Allen, H. C. *J. Phys. Chem. B* **2010**, *114*, 9485.

(82) Chen, X.; Clarke, M. L.; Wang, J. I. E.; Chen, Z. *Int. J. Mod. Phys. B* **2005**, *19*, 691.

(83) Guyot-Sionnest, P.; Hunt, J. H.; Shen, Y. R. *Phys. Rev. Lett.* **1987**, *59*, 1597.

(84) Mani, A. A.; Schultz, Z. D.; Champagne, B.; Humbert, C.; Dreesen, L.; Gewirth, A. A.; White, J. O.; Thiry, P. A.; Peremans, A.; Caudano, Y. *Appl. Surf. Sci.* **2004**, *237*, 444.

(85) Shen, Y. R.; Ostroverkhov, V. *Chem. Rev.* **2006**, *106*, 1140.

(86) Sovago, M.; Vartiainen, E.; Bonn, M. *J. Phys. Chem. C* **2009**, *113*, 6100.

(87) Wang, H.-F.; Gan, W.; Lu, R.; Rao, Y.; Wu, B.-H. *Int. Rev. Phys. Chem.* **2005**, *24*, 191.

(88) Zhuang, X.; Miranda, P. B.; Kim, D.; Shen, Y. R. *Phys. Rev. B* **1999**, *59*, 12632.

(89) Bordenyuk, A. N.; Weeraman, C.; Yatawara, A.; Jayathilake, H. D.; Stiopkin, I.; Liu, Y.; Benderskii, A. V. *J. Phys. Chem. C* **2007**, *111*, 8925.

(90) Hayes, P. L.; Keeley, A. R.; Geiger, F. M. *J. Phys. Chem. B* **2010**, *114*, 4495.

(91) Vidal, F.; Tadjeddine, A. *Rep. Prog. Phys.* **2005**, *68*, 1095.

(92) Wang, J.; Paszti, Z.; Clarke, M. L.; Chen, X.; Chen, Z. *J. Phys. Chem. B* **2007**, *111*, 6088.

(93) Watry, M. R.; Brown, M. G.; Richmond, G. L. *Appl. Spectrosc.* **2001**, *55*, 321A.

(94) Gan, W.; Wu, D.; Zhang, Z.; Feng, R. R.; Wang, H. F. *J. Chem. Phys.* **2006**, *124*, 114705.

(95) Lu, R.; Gan, W.; Wu, B.-h.; Chen, H.; Wang, H.-f. *J. Phys. Chem. B* **2004**, *108*, 7297.

(96) Korolev, N.; Allahverdi, A.; Yang, Y.; Fan, Y.; Lyubartsev, A. P.; Nordenskiöld, L. *Biophys. J.* **2010**, *99*, 1896.

(97) Špringer, T.; Šípová, H.; Vaisocherová, H.; Štěpánek, J.; Homola, J. *Nucleic Acids Res.* **2010**, *38*, 7343.